

Image-level trajectory inference of tau pathology using variational autoencoder for Flortaucipir PET

Jimin Hong (✉ jimin.hong@students.unibe.ch)

University of Bern: Universitat Bern <https://orcid.org/0000-0002-4499-2094>

Seung Kwan Kang

Seoul National University

Ian Alberts

Inselspital University Hospital Bern: Inselspital Universitatsspital Bern

Jiaying Lu

Huashan Hospital Fudan University

Raphael Sznitman

University of Bern: Universitat Bern

Jae Sung Lee

Seoul National University Hospital

Axel Rominger

Inselspital University Hospital Bern: Inselspital Universitatsspital Bern

Hongyoon Choi

Seoul National University Hospital

Kuangyu Shi

University of Bern: Universitat Bern <https://orcid.org/0000-0002-8714-3084>

Research Article

Keywords: Variational auto-encoder (VAE), Hierarchical clustering, minimum spanning tree (MST), Positron Emission Tomography (PET), [¹⁸F]Flortaucipir, Alzheimer's Disease

Posted Date: September 9th, 2021

DOI: <https://doi.org/10.21203/rs.3.rs-880967/v1>

License:  This work is licensed under a Creative Commons Attribution 4.0 International License.

[Read Full License](#)

Version of Record: A version of this preprint was published at European Journal of Nuclear Medicine and Molecular Imaging on February 28th, 2022. See the published version at <https://doi.org/10.1007/s00259->

021-05662-z.

1 **Image-level trajectory inference of tau pathology using variational**
2 **autoencoder for Flortaucipir PET**

3 Jimin Hong¹, Seung Kwan Kang², Ian Alberts¹, Jiaying Lu^{1,3}, Raphael Sznitman⁴, Jae Sung Lee², Axel
4 Rominger¹, Hongyoon Choi², Kuangyu Shi^{1,5}, and the Alzheimer's Disease Neuroimaging Initiative*

5 ¹ Department of Nuclear Medicine, Inselspital, University of Bern, Switzerland

6 ² Department of Nuclear Medicine, Seoul National University Hospital, Seoul, Republic of Korea

7 ³ PET Center, Huashan Hospital, Fudan University, China

8 ⁴ ARTORG Center, University of Bern, Switzerland

9 ⁵ Department of Informatics, Technical University of Munich, Germany

10

11 **Corresponding Author:**

Hongyoon Choi

28 Yeon Gun, Jong Ro, Seoul, South Korea
+82 2 2072 3347
chy1000@snu.ac.kr

Kuangyu Shi

Freiburgstrasse 18, 3010 Bern, Switzerland
Tel. +41 31 63 27135
Fax. +41 31 632 31 37
kuangyu.shi@dbmr.unibe.ch

12

13 **First Author:**

14 Jimin Hong

15 Freiburgstrasse 18, 3010 Bern, Switzerland
16 +41 79 761 7942
17 jimin.hong@students.unibe.ch
18

19 * Data used in preparation of this article were obtained from the Alzheimer's Disease Neuroimaging Initiative (ADNI) database
20 (adni.loni.usc.edu). As such, the investigators within the ADNI contributed to the design and implementation of ADNI and/or provided data
21 but did not participate in analysis or writing of this report. A complete listing of ADNI investigators can be found at: [http://adni.loni.usc.edu/wp-](http://adni.loni.usc.edu/wp-content/uploads/how_to_apply/ADNI_Acknowledgement_List.pdf)
22 [content/uploads/how_to_apply/ADNI_Acknowledgement_List.pdf](http://adni.loni.usc.edu/wp-content/uploads/how_to_apply/ADNI_Acknowledgement_List.pdf)

23

24

25

26 Short running title: Image-level tau trajectory in AD using VAE

27 **Abstract**

28 **Purpose:** Alzheimer's disease (AD) studies revealed that abnormal deposition of tau spreads in
29 a specific spatial pattern, namely Braak stage. However, Braak staging is based on post mortem
30 brains, each of which represents the cross-section of the tau trajectory in disease progression,
31 and numerous studies were reported that does not conform to this model. This study aimed to
32 identify the tau trajectory and additionally quantify the tau progress in a data-driven approach
33 using the continuous latent space learned by variational autoencoder (VAE).

34 **Methods:** 1080 [¹⁸F]Flortaucipir brain PET images were collected from Alzheimer's Disease
35 Neuroimaging Initiative database. VAE was built to compress the hidden features from tau
36 images in latent space. Hierarchical clustering and minimum spanning tree were applied to
37 organize the features and calibrate them to the tau progression, thus deriving *pseudo-time*. The
38 image-level tau trajectory was inferred by continuously sampling across the calibrated latent
39 features. We assessed the *pseudo-time* with regards to tau standardized uptake value ratio (SUVR)
40 in AD-vulnerable regions, amyloid deposit, glucose metabolism, cognitive scores and clinical
41 diagnosis.

42 **Results:** We identified 4 clusters that plausibly capture certain stages of AD and organized the
43 clusters in the latent space. The inferred tau trajectory agreed with the Braak staging. According
44 to the derived *pseudo-time*, tau first deposits in the parahippocampal and amygdala, and then
45 spreads to fusiform, inferior temporal lobe, and posterior cingulate. Prior to the regional tau
46 deposition, amyloid accumulates first.

47 **Conclusion:** The spatiotemporal trajectory of tau progression inferred in this study was
48 consistent with Braak staging, and the profile of other biomarkers in disease progression agreed
49 well with previous findings. We addressed that this approach additionally carries a potential to
50 quantify tau progression as a continuous variable taking a whole-brain tau image into account.

51 **Keywords:** Variational auto-encoder (VAE), Hierarchical clustering, minimum spanning tree (MST), Positron
52 Emission Tomography (PET), [¹⁸F]Flortaucipir, Alzheimer's Disease

53 **Declarations**

54

55 **Funding:** Swiss National Science Foundation (SNF) Nr. 188350, National Research
56 Foundation of Korea (NRF-2019K1A3A1A14065446), and Korea Medical Device
57 Development Fund grant funded by the Korea government (the Ministry of Science and ICT,
58 the Ministry of Trade, Industry and Energy, the Ministry of Health & Welfare, the Ministry of
59 Food and Drug Safety) (Project Number: 202011A06)

60 **Conflict of interest/Competing interests:**

61 KS receives research grants from Novartis and Siemens Healthineers, and sponsorships from
62 Novartis, Siemens Healthineers, Hermes Medical Solution, DosiSoft, Varian, THQ Medical
63 Products, QDose, PMOD, Boston Scientifics, SIRTEX, MIM Software, ICPO foundation. HC
64 is a cofounder and CTO of Portrai inc. and a scientific advisory board member for
65 AltheNutriGene.

66 **Availability of data and material:**

67 Data collection and sharing for this project was funded by the Alzheimer's Disease
68 Neuroimaging Initiative (ADNI) (National Institutes of Health Grant U01 AG024904) and
69 DOD ADNI (Department of Defense award number W81XWH-12-2-0012). ADNI is funded
70 by the National Institute on Aging, the National Institute of Biomedical Imaging and
71 Bioengineering, and through generous contributions from the following: AbbVie, Alzheimer's
72 Association; Alzheimer's Drug Discovery Foundation; Araclon Biotech; BioClinica, Inc.;
73 Biogen; Bristol-Myers Squibb Company; CereSpir, Inc.; Cogstate; Eisai Inc.; Elan
74 Pharmaceuticals, Inc.; Eli Lilly and Company; EuroImmun; F. Hoffmann-La Roche Ltd and its
75 affiliated company Genentech, Inc.; Fujirebio; GE Healthcare; IXICO Ltd.; Janssen Alzheimer
76 Immunotherapy Research & Development, LLC.; Johnson & Johnson Pharmaceutical Research
77 & Development LLC.; Lumosity; Lundbeck; Merck & Co., Inc.; Meso Scale Diagnostics, LLC.;
78 NeuroRx Research; Neurotrack Technologies; Novartis Pharmaceuticals Corporation; Pfizer

79 Inc.; Piramal Imaging; Servier; Takeda Pharmaceutical Company; and Transition Therapeutics.
80 The Canadian Institutes of Health Research is providing funds to support ADNI clinical sites in
81 Canada. Private sector contributions are facilitated by the Foundation for the National Institutes
82 of Health (www.fnih.org). The grantee organization is the Northern California Institute for
83 Research and Education, and the study is coordinated by the Alzheimer's Therapeutic Research
84 Institute at the University of Southern California. ADNI data are disseminated by the
85 Laboratory for Neuro Imaging at the University of Southern California.

86 **Code availability:**

87 Not applicable

88 **Ethics approval:**

89 Not applicable

90 **Consent to participate :**

91 Not applicable

92 **Consent for publication:**

93 Not applicable

94

95 **1. Introduction**

96
97 One of the key pathophysiologic features of Alzheimer’s disease (AD) is neurofibrillary tangles
98 (NFTs), which are formed by the hyperphosphorylation and abnormal aggregation of tau protein
99 (1). The abnormal tau pathology is related to cognitive dysfunction and predicts longitudinal
100 change in neuronal loss (2,3). Therefore, the degree of tau pathology is important to understand
101 the disease progression and can be taken to be reflective of clinical severity (4).

102
103 Post-mortem data indicate that the distribution of NFTs follows a distinctive spreading
104 pattern along with the disease progression, namely Braak stages. In the first two stages (I-II),
105 NFTs appears in the transentorhinal region, and through the limbic region (III-IV), and finally
106 in the isocortical region (V-VI) (5). However, Braak staging is based on the autopsy of the half
107 brain which shows a certain cross-section of the tau trajectory in disease progress. Recent
108 advances in positron emission tomography (PET) tracers for tau imaging allow assessment of
109 regional tau load *in vivo*, which is now a key diagnostic biomarker for the diagnosis of AD (6).
110 Of these radiotracers, [¹⁸F]flortaucipir, also known as [¹⁸F]AV-1451, has been studied widely
111 and recently approved by FDA (7). Although numerous [¹⁸F]flortaucipir PET studies agree to
112 the Braak staging (8-10), other findings argue otherwise (11-13). For instance, tau burden in
113 medial temporal regions was also addressed commonly in CN subjects (14). Additionally, the
114 clinical variants of AD affect the patterns of tau deposition (15-20).

115
116 Due to the region-specific and variable patterns of tau PET, no consensus has been made
117 on how to quantify tau PET scans and incorporate them into the A/T/N scheme – a
118 recommended category of AD biomarkers (A: β -amyloid biomarkers; T: tau biomarkers; N;
119 neurodegeneration or neuronal injury biomarkers) (6), as the region-of-interest (ROI) can be
120 defined in various ways; and this can significantly influence study outcomes (21,22). The most

121 agreed method for tau quantification is measuring the standardized uptake value ratio (SUVr)
122 in the predefined region-of-interest (ROI) assuming that the topography of tau PET deposition
123 matches well with the Braak stage (8). The AD-vulnerable ROIs, in this sense, include the
124 entorhinal, amygdala, parahippocampal, fusiform, inferior temporal, and middle temporal
125 regions (23,24). Likewise, the quantification using the combination of AD-vulnerable ROIs was
126 used in some studies, one of which classifies tau in multi-stages rather than merely rating
127 positive/negative (9). However, with accumulated evidence of the various spatiotemporal tau
128 patterns and trajectories, simple region-specific quantification of tau PET can be considered
129 less effective.

130

131 Here, we propose a data-driven model to infer an image-level spatial progression pattern
132 of tau pathology in AD, and address that this method, additionally, holds the potential to
133 quantify the degree of tau deposition as a continuous value taking the whole-brain tau image
134 into account. We hypothesized that latent, or hidden, patterns inherently exist in tau PET images.
135 These latent features were used to build a trajectory and to mark the extent of tau progression,
136 which we refer to as *pseudo-time* in this work. We derived the spatiotemporal pattern of tau
137 progression at the image-level by a deep learning model. More specifically, variational
138 autoencoder (VAE), which is an unsupervised generative model (25), hierarchical clustering
139 and minimum spanning tree (MST) was exploited for the proposed method. The tau SUVr in
140 AD-vulnerable region, amyloid deposit, glucose metabolism, cognitive scores and clinical
141 diagnosis were analyzed with regards to the discovered tau PET-based clusters and derived
142 *pseudo-time*.

143

144 **2. Material and Methods**

145

146 **Data acquisition**

147 Data used in the preparation of this article were obtained from the Alzheimer's Disease
148 Neuroimaging Initiative (ADNI) database (adni.loni.usc.edu). The ADNI was launched in 2003
149 as a public-private partnership, led by Principal Investigator Michael W. Weiner, MD. The
150 primary goal of ADNI has been to test whether serial magnetic resonance imaging (MRI),
151 positron emission tomography (PET), other biological markers, and clinical and
152 neuropsychological assessment can be combined to measure the progression of mild cognitive
153 impairment (MCI) and early Alzheimer's disease (AD). For up-to-date information, see
154 www.adni-info.org. 1080 pairs of T1 MRI image and [¹⁸F]Flortaucipir PET were recruited in
155 total, of which 78 was diagnosed as AD, 483 was as MCI, 519 was as CN in their most current
156 diagnosis. The demographics of the subjects are summarized in Table 1.

157

158 **Preprocessing**

159 All images underwent ADNI preprocessing pipeline. Every 6 five-minute frames of PET were
160 averaged and reoriented into a standard $160 \times 160 \times 96$ voxel image grid, having 1.5 mm^3 cubic
161 voxels. Each image set is filtered with a scanner-specific filter function to produce images of a
162 uniform isotropic resolution of 8 mm FWHM. Each [¹⁸F]Flortaucipir PET image was co-
163 registered to the corresponding T1 MRI image by applying a normalized mutual-information-
164 based rigid registration. MRI images were then spatially normalized to T1 MR template
165 matching the Montreal Neurological Institute (MNI) space using statistical parametric mapping
166 (SPM8, www.fil.ion.ucl.ac.uk/spm). Combining the transformation matrices of the PET-to-
167 MRI rigid registration and the MRI-to-MNI elastic registration space, the PET images were,
168 finally, spatially normalized into the MNI template. Each PET image was divided by mean tau
169 uptake of the cerebellum before being fed into the model.

170

171 **Variational autoencoder (VAE)**

172 VAE was exploited to encode the [¹⁸F]Flortaucipir PET images into the latent space and
173 generate the tau progression images inferred from the latent space, as illustrated in Figure 1A.
174 As one of the techniques to reduce dimensionality, VAE compresses the input data into
175 concentrated features, or latent features, in a smaller dimension. However, contrary to
176 independent component analysis (ICA), principal component analysis (PCA), or standard
177 autoencoder (AE), VAE encodes the input data as a distribution instead of a point and
178 regularizes the latent space by limiting the distribution produced by the encoder to be Gaussian.
179 Therefore, VAE is capable of generating a new instance by sampling from the continuous latent
180 space which is composed of a mixture of distribution. The detailed VAE algorithm is explained
181 in the Supplementary Material.

182

183 In this work, the encoder and generator were built using six convolutional layers, and
184 the latent feature dimension is of size 512, as illustrated in Figure 1B. The network was trained
185 with 540 [¹⁸F]Flortaucipir PET images for 100 epochs.

186

187 **Latent feature clustering analysis**

188 The latent features of each 1080 [¹⁸F]Flortaucipir PET were categorized using hierarchical
189 agglomerative clustering. The clustering result was plotted by T-distributed stochastic
190 neighbour embedding (t-SNE), which enables the latent feature in a dimension of 100 to be
191 visualized in 2 dimensions.

192

193 The AD-vulnerable region tau SUV_r, with cerebellum grey matter as a reference region,
194 was evaluated between the clusters, which included inferior temporal lobe (temporal_inf),
195 amygdala, parahippocampal, hippocampus, fusiform and posterior cingulum (cingulum_post)

196 defined by Automated Anatomical Labeling (AAL) atlas.

197

198 In addition, the age, Mini-Mental Status Examination (MMSE) score, [¹⁸F]AV45 SUVr,
199 [¹⁸F]FDG SUVr, and APOE4 status were analyzed between the clusters, all of which are
200 collected from ADNI data archive for each subject. The MMSE score, [¹⁸F]AV45 and [¹⁸F]FDG
201 PET SUVr was investigated to compare global cognitive function, amyloid load, and brain
202 metabolism, respectively. [¹⁸F]AV45 SUVr is defined as the mean SUVr of ROIs, including
203 frontal, anterior cingulate, precuneus, and parietal cortex, with the whole cerebellum outlined
204 by Freesurfer as a reference region (26). Similarly, [¹⁸F]FDG PET quantification data were
205 calculated by the average [¹⁸F]FDG SUVr of angular, temporal, and posterior cingulate,
206 normalized by pons/vermis reference region mean (27).

207

208 The significance of the cluster difference in clinical status was evaluated using the Chi-
209 Squared analysis for the categorical clinical phenotype variables. One-way analysis of variance
210 (ANOVA) was performed for continuous clinical phenotype variables, followed by Tukey's
211 *post hoc* pairwise test for multiple comparisons.

212

213 **Trajectory inference using minimum spanning tree (MST)**

214 The identified clusters were thought to represent a certain stage in tau progression, and MST
215 was performed to find the connection or the order of clusters. MST is defined as a weighted,
216 undirected subset of edges in a network that connects all nodes with the minimum possible total
217 edge weight without cycles.

218

219 In this work, we assumed that the clusters adjacent to one another in latent space share
220 more than the ones apart and that the progression from one cluster to another is more likely to
221 take place in the direction where the total distance is the shortest. Accordingly, we applied MST

222 in latent space, by defining nodes as the centres of the identified clusters and edge weights as
223 the euclidean distance between the corresponding pair of cluster centres.

224

225 The derived MST graph was used as a calibration to measure the tau progression,
226 corresponding the nodes to the marks and the edge weight to the distances between the marks.
227 The latent features were sampled continuously across the edges of the resulting MST graph in
228 order of tau progression, and the image-level tau trajectory was inferred by the trained VAE
229 generator.

230

231 **Pseudo-time**

232 In addition, we defined the *pseudo-time* of each tau image that describes the extent of
233 tau progression as a continuous value in a range of 0-100, which is measured by the geometrical
234 relationship between its latent feature and the derived MST graph in latent space. For each tau
235 image, we first calculated its latent vector relative to its cluster centre and projected this vector
236 onto the corresponding edge in MST graph, and measured the scalar projection to pinpoint the
237 location. The points marked by each latent feature were normalized and scaled in a range of 0-
238 100, which we refer to as *pseudo-time*.

239

240 The regional tau uptake and various biomarker information, retrieved from ADNI data
241 archive, were outlined with regards to derived *pseudo-time*. In order to estimate the *pseudo-*
242 *time* at which SUVr of regional tau PET as well as other biomarker PET significantly changes,
243 we regressed the *pseudo-time* SUVr curves to the logistic model.

244

245 Moreover, we calculated the length between each latent feature and the respective edge
246 in MST graph and flagged the outliers that were fallen outside of the 95 percentile in order to
247 potentially detect the atypical tau patterns. The tau patterns of the outliers were examined.

248 **3. Results**

249

250 **Clusters identification**

251 We identified 4 clusters from the latent features encoded by VAE and hierarchical
252 agglomerative clustering. Figure 2A-B illustrates the clustering result and the diagnosis of 1080
253 data respectively in the t-SNE plot. The heatmap of the contingency table is shown in Figure
254 2C, which depicts the ratio of diagnosis within each cluster. AD subjects were not found in
255 cluster 3, whereas prevalent in cluster 2. MCI subjects were found mostly in cluster 0 and cluster
256 2. The difference of ratio between cluster 1 and cluster 3 was subtle.

257

258 **Standardized uptake value ratio (SUVr) in ROI between clusters and Braak stages**

259 Figure 3A depicts the average tau PET image of each cluster, normalized by average uptake in
260 cerebellum grey matter. In average, tau deposition gradually increased in temporal lobe and
261 frontal lobe in the order of cluster 3, cluster 1, cluster 0 and cluster 2. Figure 3B illustrates the
262 tau SUVr within ROIs in AD-vulnerable ROIs. Across AD-vulnerable regions, cluster 2
263 presented the highest average SUVr, except for hippocampus where cluster 1 showed the
264 highest. Supplementary Table 1 shows the results from ANOVA and Tukey's pairwise test in
265 temporal and cingulate ROIs defined in AAL template. In most ROIs, the group difference
266 between cluster 0, cluster 1, and cluster 3 was trivial, except for amygdala where cluster 0
267 presented significantly more tau deposition than cluster 3. Thus, cluster 2 was regarded as a
268 typical AD with advanced tau depositions, while the other three clusters represented normal or
269 early tau pathology progression.

270

271 **Clinical variance between the clusters**

272 Table 2 summarized the clinical variance between the clusters. The average age was lowest in
273 cluster 3, and no pronounced difference was found in the average age between other clusters.

274 The average MMSE score was lowest in cluster 2, and second lowest in cluster 0, but no
275 difference was found between cluster 1 and cluster 3. The average [¹⁸F]AV45 PET SUVr was
276 the highest in cluster 2, but no significant difference was found between other three clusters.
277 The average [¹⁸F]FDG PET SUVr was lowered in the order of cluster 3, 1, 0, and 2, however,
278 Tukey's test indicated no difference between cluster 1 and cluster 3. APOE4-positive cases were
279 prevalent in cluster 2, and less common in cluster 3, followed by cluster 0 and cluster 1. Female
280 subjects were more included in cluster 3, and less included in cluster 0.

281

282 **MST and inference of tau trajectory**

283 The MST method resulted in a straight graph with cluster 1 and cluster 2 as leaf nodes as shown
284 in Figure 4A. Although MST is an undirected graph and does not provide the starting and
285 endpoint of the network, we determined cluster 1 as the initial node of tau progression and
286 cluster 2 as the last node, given the regional tau uptake and the clinical variance between the
287 clusters. Accordingly, the series of cluster 1, cluster 3, cluster 0, and cluster 2 was established
288 as a tau progress sequence. The latent vector trajectory was derived by continuously sampling
289 the edges through the defined MST graph, and the tau PET trajectory was reproduced using
290 MST generator as shown in Figure 4B, and the video is provided in *supplementary materials*.
291 Similar to Braak stages, the tau deposits initially in medial temporal lobe and gradually to
292 temporal lobe and frontal lobe.

293

294 **Pseudo-time analysis**

295 The *pseudo-time* was measured for each tau-images. Figure 5A depicts the comparison of
296 *pseudo-time* between different diagnosis groups. AD group showed higher *pseudo-time* than
297 CN group, and the MCI group showed a broader range of *pseudo-time*. Figure 5B illustrates the
298 derived *pseudo-time* in t-SNE plot. Figure 5C depicts the profile of amyloid deposit estimated
299 by [¹⁸F]AV45 PET together with glucose metabolism estimated by [¹⁸F]FDG PET with regards

300 to *pseudo-time*. The amyloid deposit gradually increased throughout *pseudo-time*, whereas
301 glucose metabolism stayed stable. Figure 5D shows the MMSE score and figure 5E illustrates
302 tau SUVR profiles in AD-vulnerable ROIs regarding *pseudo-time*. The profile of fusiform,
303 cingulum_post, and temporal_inf appeared similar, where drastic upturn was found in the tail
304 of *pseudo-time*. The outline of hippocampus stayed unchanged and that of amygdala and
305 parahippocampal showed consistent increase. The MMSE declined around *pseudo-time* of 60.
306 The logistic regression of figure 5C and 5E is illustrated in Supplementary Figure 1. The
307 amyloid deposit calculated by [¹⁸F]AV45 PET first increased, and the tau SUVR in AD-
308 vulnerable regions escalated later. More specifically, the tau SUVR of parahippocampal first
309 started to increase, followed by amygdala, fusiform, temp_inf and cingulum_post. However,
310 the tau SUVR of hippocampus rather decreased, and [¹⁸F]FDG SUVR increased, which was
311 poorly estimated.

312

313 In addition, the atypical tau pattern was acquired and the examples are introduced in
314 Supplementary Figure 2. According to the method we applied, there was no indication of any
315 atypical tau pattern in cluster 3. The examples included the patterns from cluster 0, cluster 1,
316 and cluster 2.

317

318 **4. Discussion**

319 For decades, the trajectory of tau pathology has been primarily studied upon a single model,
320 Braak stages, while numerous cases were reported that do not conform. Besides the model being
321 region-specific, these variants of tau trajectories added extra challenges to quantifying the
322 progress of tau in AD. Recently, the trajectory of tau deposition was extensively studied and the
323 four distinctive trajectories were identified (20). In parallel, efforts were made to find the best
324 quantification scheme to account for tau PET scans in AD (23, 24). We employed a deep
325 learning algorithm to infer the tau trajectory without any prior knowledge, and came along with
326 the *pseudo-time* of tau progress, which quantifies the extent of tau deposit in disease progression
327 at individual level. Our finding reassured the Braak’s model, and demonstrated that *pseudo-*
328 *time* potentially solve the challenges in tau quantification, as it takes the whole brain tau PET
329 itself into consideration and delivers the continuous tau progress index.

330

331 Upon building the tau trajectory, we detected the *atypical* asymmetric tau pattern
332 depicted in Supplementary Figure 2. Aside from the *typical* presentation of tau pathology from
333 the medial temporal regions and resulted impairment of episodic memory, studies have found
334 *atypical* tau patterns and their related clinical symptoms, such as primary progressive aphasia
335 (PPA) or posterior cortical atrophy (PCA) (28). Although various *atypical* tau patterns and its
336 trajectories were found in the other research group (20), we focused on deriving the *typical* tau
337 trajectory and flagged the outliers as simply *atypical* tau pattern in this work. However, we
338 believe that this method could contribute to the extensive search on *atypical* tau trajectories and
339 their related symptoms, if provided with further clinical notes of the subjects in the future.

340

341 Additionally, we addressed that this approach has the potential to quantify tau progress
342 as a continuous value, which we refer to as *pseudo-time*, taking the whole-brain tau image into
343 account. One of the challenges that the *priori* ROI-based quantification faces is its limitation in

344 reflecting the various and atypical spatial patterns of tau accumulation in PET (28, 29).
345 Furthermore, image noise and quantification errors hinder the performance of the ROI-based
346 quantification method at the early stage of tau pathology with mild tau accumulation. Our
347 method dealt with this concern by employing the renowned deep learning algorithm, VAE, and
348 using whole-brain tau image as an input. VAE serves as the model to learn non-linear dimension
349 reduction functions of higher dimension PET images. The latent vectors in autoencoder (AE)
350 tends to be uninterpretable as AE finds the latent vector which merely reconstructs the input as
351 similar as possible. On the other hand, VAE encodes the latent features by regularizing the latent
352 space to be continuous, hence, allowing to generate new data by sampling from its latent space.
353 The reason behind selecting VAE lies in its capacity to form a continuous latent space for the
354 distribution of tau PET image hence deriving better quantification result.

355

356 Moreover, deriving the *pseudo-time* helps to better understand the complementary
357 information of tau regional uptake and various PET biomarkers, including amyloid pathology
358 and brain metabolism. For instance, our finding agrees that the accumulation rate, especially in
359 inferior temporal lobe, can be alternatively a good indicator, which was also suggested by the
360 longitudinal tau PET study from the other group (12). Earlier to the regional tau uptakes taking
361 place, amyloid PET uptake starts increasing first. This consequence of biomarker corresponds
362 to the previously well-known hypothesis of dynamic biomarkers of AD pathological cascade
363 (30, 31). However, the *pseudo-time* for hippocampus is poorly estimated. We speculate that the
364 misleading result might come from the brain atrophy. Similarly, the logistic regression for FDG
365 *pseudo-time* curve is conflicting, as it rather increases throughout *pseudo-time*. This comes from
366 the lack of information in ADNI, and the distribution of FDG *pseudo-time* curve was
367 comparatively sparse.

368

369 The methodological limitation remains in each building block of this study. Although

370 the VAE worked well with our purposes, the outputs generated from the VAE for trajectory
371 analysis were blurry, which is known to be common (32). Another limitation for this work is
372 the heuristic setting in the number of resulting clusters. That is, we fixed the number of clusters
373 manually in order to avoid overfitting and underfitting problem, referring to the dendrogram,
374 distance plot, t-SNE plot and diagnosis contingency matrix. MST has been a popular choice in
375 brain network or connectivity studies mostly in fMRI studies (33, 34), and was recently
376 introduced in AD disease progression study using gene expression data (35). To our best
377 knowledge, MST has not yet been explored in brain PET imaging to model the trajectory of
378 disease progression in AD. In our study, MST showed the potential to discover the relationship
379 between the tau PET clusters, hence, the tau trajectory. Furthermore, we observed the nested
380 sub-network in MST with a larger number of clusters. This can indicate that if our method is
381 expanded to a larger number of clusters, the distinctive subtypes of the tau trajectories can be
382 identified together with its *pseudo-time*. However, as an undirected graph, starting and ending
383 point is not determined by MST, and this opens more place for the discussion in the
384 interpretation of the result derived by a larger number of clusters.

385

386 In accordance with the remark we made, future studies will aim to expand our model to
387 identify the various trajectories and their *pseudo-time*, as well as the related clinical symptoms.
388 In this work, we simply detected the *atypical* pattern, but we believe the extensive tau
389 trajectories can be found and quantified with our model if well developed.

390

391 **5. Conclusion**

392 In this work, we identified the image-level tau trajectory without any prior knowledge of
393 existing models such as Braak stages, using VAE, hierarchical clustering, and MST.
394 Additionally, we addressed that this approach has the potential to quantify tau progress as a
395 continuous value, which we refer to as *pseudo-time*. This method, contrary to the ROI-based
396 quantification method, considers the whole brain image to pinpoint the extent of tau progress
397 at the individual level. Furthermore, *pseudo-time* can guide the better understanding of the
398 association between tau burden and other biomarkers such as amyloid, neuronal injury in the
399 pathophysiology of AD. Importantly, atypical tau patterns were detected upon deriving tau
400 trajectory, and we believe this approach sheds new light on an extensive search of distinctive
401 tau trajectories as well as its quantification.

402

403 References

404 1. Okamura N, Harada R, Ishiki A, Kikuchi A, Nakamura T, Kudo Y. The development and
405 validation of tau PET tracers: current status and future directions. *Clin Transl Imaging*.
406 2018;6:305–16. <https://doi.org/10.1007/s40336-018-0290-y>

407

408 2. La Joie R, Bejanin A, Fagan AM, Ayakta N, Baker SL, Bourakova V, et al. Associations
409 between [18F]AV1451 tau PET and CSF measures of tau pathology in a clinical sample.
410 *Neurology*. 2018;90:e282–90. <https://doi.org/10.1212/WNL.0000000000004860>

411

412 3. R LJ, Av V, Sl B. Prospective longitudinal atrophy in Alzheimer’s disease correlates with
413 the intensity and topography of baseline tau-PET. *Sci Transl Med*. 2020;12. .
414 <https://doi.org/10.1126/scitranslmed.aau5732>

415

416 4. Gordon BA, Blazey TM, Christensen J, Dincer A, Flores S, Keefe S, et al. Tau PET in
417 autosomal dominant Alzheimer’s disease: relationship with cognition, dementia and other
418 biomarkers. *Brain*. 2019;142:1063–76. <https://doi.org/10.1093/brain/awz019>

419

420 5. Braak H, Braak E. Neuropathological staging of Alzheimer-related changes. *Acta*
421 *Neuropathol*. 1991;82:239–59. <https://doi.org/10.1007/BF00308809>

422

423 6. Jack CR Jr, Bennett DA, Blennow K, Carrillo MC, Dunn B, Haeberlein SB, et al. NIA-AA
424 Research Framework: Toward a biological definition of Alzheimer’s disease. *Alzheimers*
425 *Dement*. 2018;14:535–62. <https://doi.org/10.1016/j.jalz.2018.02.018>

426

427 7. Mattay VS, Fotenos AF, Ganley CJ, Marzella L. Brain tau imaging: Food and drug
428 administration approval of 18F-flortaucipir injection. *J Nucl Med*. 2020;61:1411–2.
429 <https://doi.org/10.2967/jnumed.120.252254>

430

431 8. Cho H, Choi JY, Hwang MS, Kim YJ, Lee HM, Lee HS, et al. In vivo cortical spreading
432 pattern of tau and amyloid in the Alzheimer disease spectrum. *Ann Neurol*. 2016;80:247–58.
433 <https://doi.org/10.1002/ana.24711>

434

- 435 9. Schöll M, Lockhart SN, Schonhaut DR, O’Neil JP, Janabi M, Ossenkoppele R, et al. PET
436 imaging of tau deposition in the aging human brain. *Neuron*. 2016;89:971–82.
437 <https://doi.org/10.1016/j.neuron.2016.01.028>
- 438
- 439 10. Schwarz AJ, Yu P, Miller BB, Shcherbinin S, Dickson J, Navitsky M, et al. Regional
440 profiles of the candidate tau PET ligand 18F-AV-1451 recapitulate key features of Braak
441 histopathological stages. *Brain*. 2016;139:1539–50. <https://doi.org/10.1093/brain/aww023>
- 442
- 443 11. Jones DT, Knopman DS, Gunter JL, Graff-Radford J, Vemuri P, Boeve BF, et al. Cascading
444 network failure across the Alzheimer’s disease spectrum. *Brain*. 2016;139:547–62.
445 <https://doi.org/10.1093/brain/awv338>
- 446
- 447 12. Jack CR Jr, Wiste HJ, Schwarz CG, Lowe VJ, Senjem ML, Vemuri P, et al. Longitudinal
448 tau PET in ageing and Alzheimer’s disease. *Brain*. 2018;141:1517–28.
449 <https://doi.org/10.1093/brain/awy059>
- 450
- 451 13. Leuzy A, Chiotis K, Lemoine L, Gillberg P-G, Almkvist O, Rodriguez-Vieitez E, et al. Tau
452 PET imaging in neurodegenerative tauopathies-still a challenge. *Mol Psychiatry*.
453 2019;24:1112–34. <https://doi.org/10.1038/s41380-018-0342-8>
- 454
- 455 14. Crary JF, Trojanowski JQ, Schneider JA, Abisambra JF, Abner EL, Alafuzoff I, et al.
456 Primary age-related tauopathy (PART): a common pathology associated with human aging.
457 *Acta Neuropathol*. 2014;128:755–66. <https://doi.org/10.1007/s00401-014-1349-0>
- 458
- 459 15. Ossenkoppele R, Schonhaut DR, Schöll M, Lockhart SN, Ayakta N, Baker SL, et al. Tau
460 PET patterns mirror clinical and neuroanatomical variability in Alzheimer’s disease. *Brain*.
461 2016;139:1551–67. <https://doi.org/10.1093/brain/aww027>
- 462
- 463 16. Schöll M, Ossenkoppele R, Strandberg O, Palmqvist S, Swedish BioFINDER study, Jögi J,
464 et al. Distinct 18F-AV-1451 tau PET retention patterns in early- and late-onset Alzheimer’s
465 disease. *Brain*. 2017;140:2286–94. <https://doi.org/10.1093/brain/awx171>
- 466
- 467 17. Ossenkoppele R, Pijnenburg YAL, Perry DC, Cohn-Sheehy BI, Scheltens NME, Vogel JW,
468 et al. The behavioural/dysexecutive variant of Alzheimer’s disease: clinical, neuroimaging and
469 pathological features. *Brain*. 2015;138:2732–49. <https://doi.org/10.1093/brain/awv191>

470

471 18. Gorno-Tempini ML, Hillis AE, Weintraub S, Kertesz A, Mendez M, Cappa SF, et al.
472 Classification of primary progressive aphasia and its variants. *Neurology*. 2011;76:1006–14.
473 <https://doi.org/10.1212/WNL.0b013e31821103e6>

474

475 19. Crutch SJ, Schott JM, Rabinovici GD, Murray M, Snowden JS, van der Flier WM, et al.
476 Consensus classification of posterior cortical atrophy. *Alzheimers Dement*. 2017;13:870–84.
477 <https://doi.org/10.1016/j.jalz.2017.01.014>

478

479 20. Vogel JW, Young AL, Oxtoby NP, Smith R, Ossenkoppele R, Strandberg OT, et al. Four
480 distinct trajectories of tau deposition identified in Alzheimer's disease. *Nat Med*. 2021;27:871–
481 81. <https://doi.org/10.1038/s41591-021-01309-6>

482

483 21. Maass A, Landau S, Baker SL, Horng A, Lockhart SN, La Joie R, et al. Comparison of
484 multiple tau-PET measures as biomarkers in aging and Alzheimer's disease. *Neuroimage*.
485 2017;157:448–63. <https://doi.org/10.1016/j.neuroimage.2017.05.058>

486

487 22. Mishra S, Gordon BA, Su Y, Christensen J, Friedrichsen K, Jackson K, et al. AV-1451 PET
488 imaging of tau pathology in preclinical Alzheimer disease: Defining a summary measure.
489 *Neuroimage*. 2017;161:171–8. <https://doi.org/10.1016/j.neuroimage.2017.07.050>

490

491 23. Wang L, Benzinger TL, Su Y, Christensen J, Friedrichsen K, Aldea P, et al. Evaluation of
492 tau imaging in staging Alzheimer disease and revealing interactions between β -amyloid and
493 tauopathy. *JAMA Neurol*. 2016;73:1070. <https://doi.org/10.1001/jamaneurol.2016.2078>

494

495 24. Jack CR Jr, Wiste HJ, Weigand SD, Therneau TM, Lowe VJ, Knopman DS, et al. Defining
496 imaging biomarker cut points for brain aging and Alzheimer's disease. *Alzheimers Dement*.
497 2017;13:205–16. <https://doi.org/10.1016/j.jalz.2016.08.005>

498

499 25. Kingma DP, Welling M. Auto-Encoding Variational Bayes [Internet]. arXiv [stat.ML].
500 2013. <http://arxiv.org/abs/1312.6114>

501

502 26. Landau SM, Lu M, Joshi AD, Pontecorvo M, Mintun MA, Trojanowski JQ, et al.
503 Comparing positron emission tomography imaging and cerebrospinal fluid measurements of β -

504 amyloid: CSF and Amyloid PET Imaging. *Ann Neurol.* 2013;74:826–36.
505 <https://doi.org/10.1002/ana.23908>

506

507 27. Landau SM, Harvey D, Madison CM, Koeppe RA, Reiman EM, Foster NL, et al.
508 Associations between cognitive, functional, and FDG-PET measures of decline in AD and MCI.
509 *Neurobiol Aging.* 2011;32:1207–18. <https://doi.org/10.1016/j.neurobiolaging.2009.07.002>

510

511 28. Sarazin M, Lagarde J, Bottlaender M. Distinct tau PET imaging patterns in typical and
512 atypical Alzheimer’s disease. *Brain.* 2016;139:1321–4. <https://doi.org/10.1093/brain/aww041>

513

514 29. Xia C, Makaretz SJ, Caso C, McGinnis S, Gomperts SN, Sepulcre J, et al. Association of
515 in vivo [18F]AV-1451 tau PET imaging results with cortical atrophy and symptoms in typical
516 and atypical Alzheimer disease. *JAMA Neurol.* 2017;74:427–36.
517 <https://doi.org/10.1001/jamaneuro.2016.5755>

518

519 30. Jack CR Jr, Knopman DS, Jagust WJ, Shaw LM, Aisen PS, Weiner MW, et al. Hypothetical
520 model of dynamic biomarkers of the Alzheimer’s pathological cascade. *Lancet Neurol.*
521 2010;9:119–28. [https://doi.org/10.1016/S1474-4422\(09\)70299-6](https://doi.org/10.1016/S1474-4422(09)70299-6)

522

523 31. Chételat G, Arbizu J, Barthel H, Garibotto V, Law I, Morbelli S, et al. Amyloid-PET and
524 18F-FDG-PET in the diagnostic investigation of Alzheimer’s disease and other dementias.
525 *Lancet Neurol.* 2020;19:951–62. [https://doi.org/10.1016/S1474-4422\(20\)30314-8](https://doi.org/10.1016/S1474-4422(20)30314-8)

526

527 32. Zhao S, Song J, Ermon S. Towards deeper understanding of variational autoencoding
528 models [Internet]. arXiv [cs.LG]. 2017. <http://arxiv.org/abs/1702.08658>

529

530 33. Stam CJ, Tewarie P, Van Dellen E, van Straaten ECW, Hillebrand A, Van Mieghem P. The
531 trees and the forest: Characterization of complex brain networks with minimum spanning trees.
532 *Int J Psychophysiol.* 2014;92:129–38. <https://doi.org/10.1016/j.ijpsycho.2014.04.001>

533

534 34. Tewarie P, Hillebrand A, Schoonheim MM, van Dijk BW, Geurts JJG, Barkhof F, et al.
535 Functional brain network analysis using minimum spanning trees in Multiple Sclerosis: an
536 MEG source-space study. *Neuroimage.* 2014;88:308–18.
537 <https://doi.org/10.1016/j.neuroimage.2013.10.022>

538

539 35. Iturria-Medina Y, Khan AF, Adewale Q, Shirazi AH, Alzheimer's Disease Neuroimaging
540 Initiative. Blood and brain gene expression trajectories mirror neuropathology and clinical
541 deterioration in neurodegeneration. *Brain*. 2020;143:661–73.
542 <https://doi.org/10.1093/brain/awz400>

543

544

545 **Table 1** The demographics of the subjects.

546

	AD (n = 78)	MCI (n = 483)	CN (n = 519)	TOTAL (n = 1080)
Age (years)	74.8 ± 8.4	74.7 ± 7.4	74.4 ± 7.7	74.6 ± 7.6
Sex (M : F)	46 :32	254 : 229	216 : 303	516 : 564
APOE4* (positive %)	61.9	43.8	36.1	44.6
MMSE**	21.9 ± 4.3	27.5 ± 3.2	28.9 ± 1.4	27.8 ± 3.2
Education (years)	15.3 ± 2.6	16.4 ± 2.5	16.6 ± 2.4	16.4 ± 2.5

547

548

549 *Apolipoprotein E. We defined the subject carrying either APOE3/4 or APOE4/4 as positive case.

550 ** Mini-Mental State Examination (MMSE)

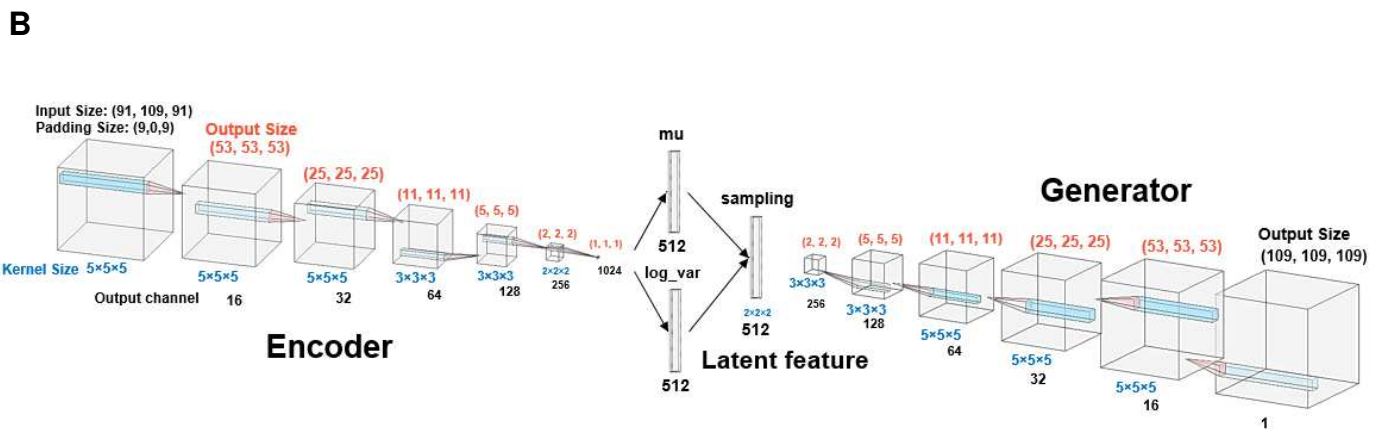
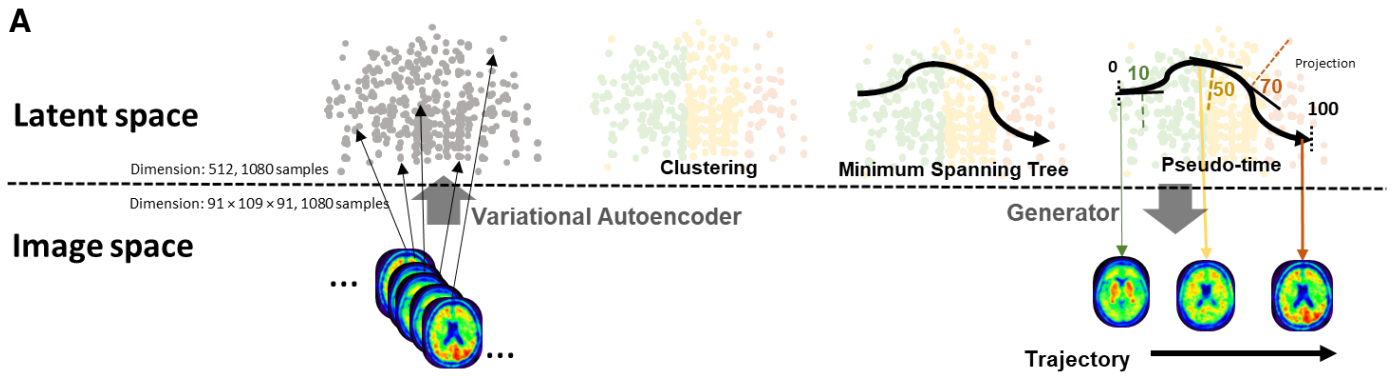
551

552

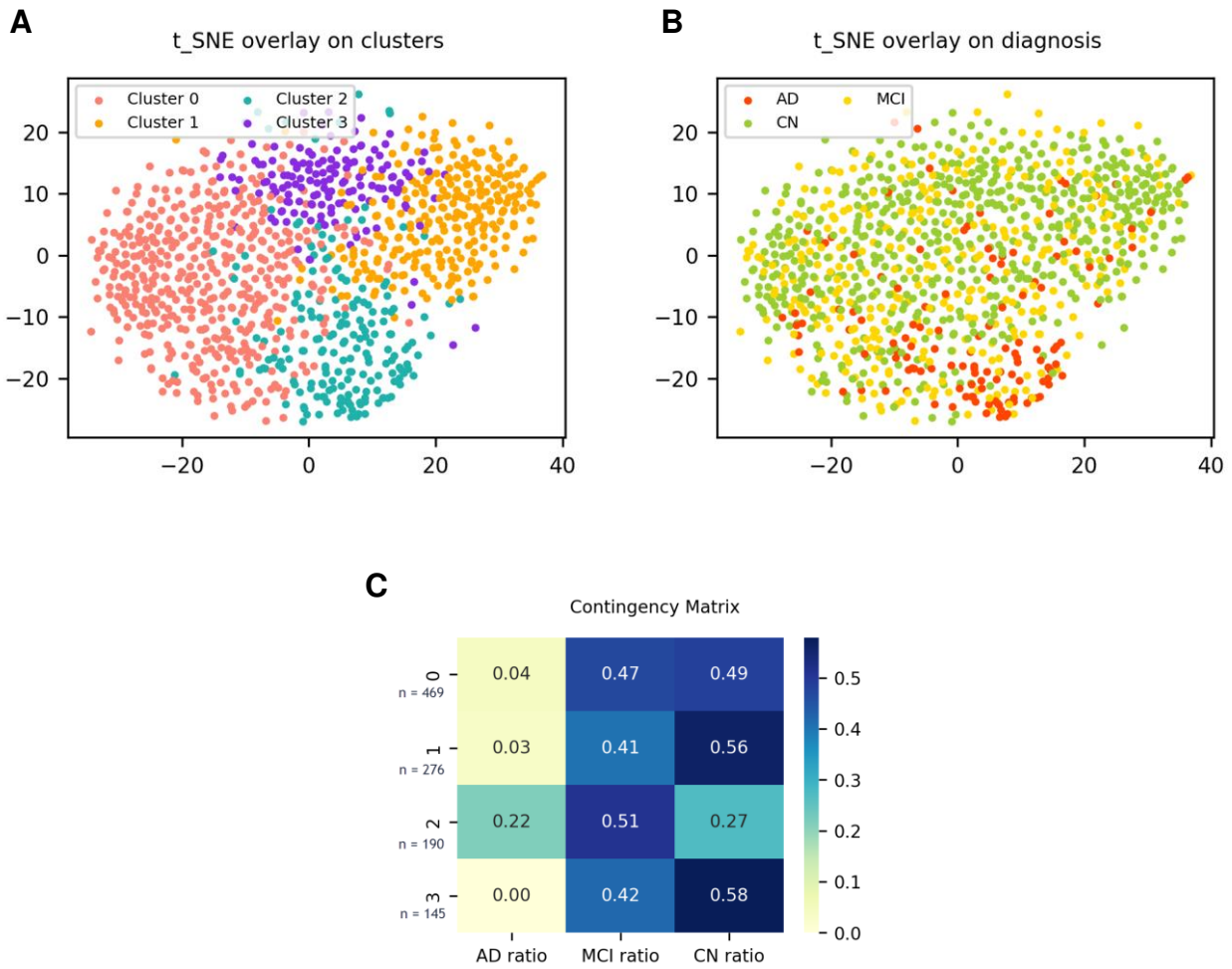
553 **Table 2** The statistical differences of Age, MMSE, [18F]AV45, FDG, Sex and APOE status between each
 554 clusters

	<i>Age</i>	<i>MMSE</i>	<i>[18F]AV45</i>	<i>[18F]FDG</i>	<i>Sex (F)</i>	<i>APOE (positive)</i>
Cluster_0	74.79 ± 7.16	28.06 ± 2.72	1.14 ± 0.20	1.22 ± 0.14	43.92%	38.76%
Cluster_1	75.03 ± 7.84	28.56 ± 2.02	1.13 ± 0.19	1.27 ± 0.11	59.42%	36.07%
Cluster_2	76.13 ± 8.11	24.98 ± 4.66	1.37 ± 0.25	1.09 ± 0.12	51.57%	52.94%
Cluster_3	70.77 ± 6.64	28.95 ± 1.19	1.11 ± 0.17	1.30 ± 0.10	66.20%	43.79%
test value(F/chi2)	15.78	74.12	31.96	26.04	30.07	13.88
p vlaue	< 0.001	< 0.001	< 0.001	< 0.001	< 0.001	< 0.01
Tukey's test significance	[0,3], [1,3], [2,3]	[0,2], [0,3], [1,2], [2,3]	[0,2], [1,2], [2,3]	[0,2], [0,3], [1,2], [2,3]		

555



556
 557 **Figure 1 Study design and model architect for variational autoencoder (VAE).** **A.** The scheme of the
 558 study design. The tau brain images were first embedded into the latent feature by VAE, and those latent
 559 features were clustered by hierarchical agglomerative clustering. The identified clusters were organized by
 560 minimum spanning tree (MST), and the tau trajectory was reproduced using VAE generator by continuously
 561 sampling across the MST graph. *Pseudo-time* was defined to mark the degree of the tau progression. **B.** VAE
 562 architecture. 6 convolving layers were built for both encoder and generator, with the latent size of 512.

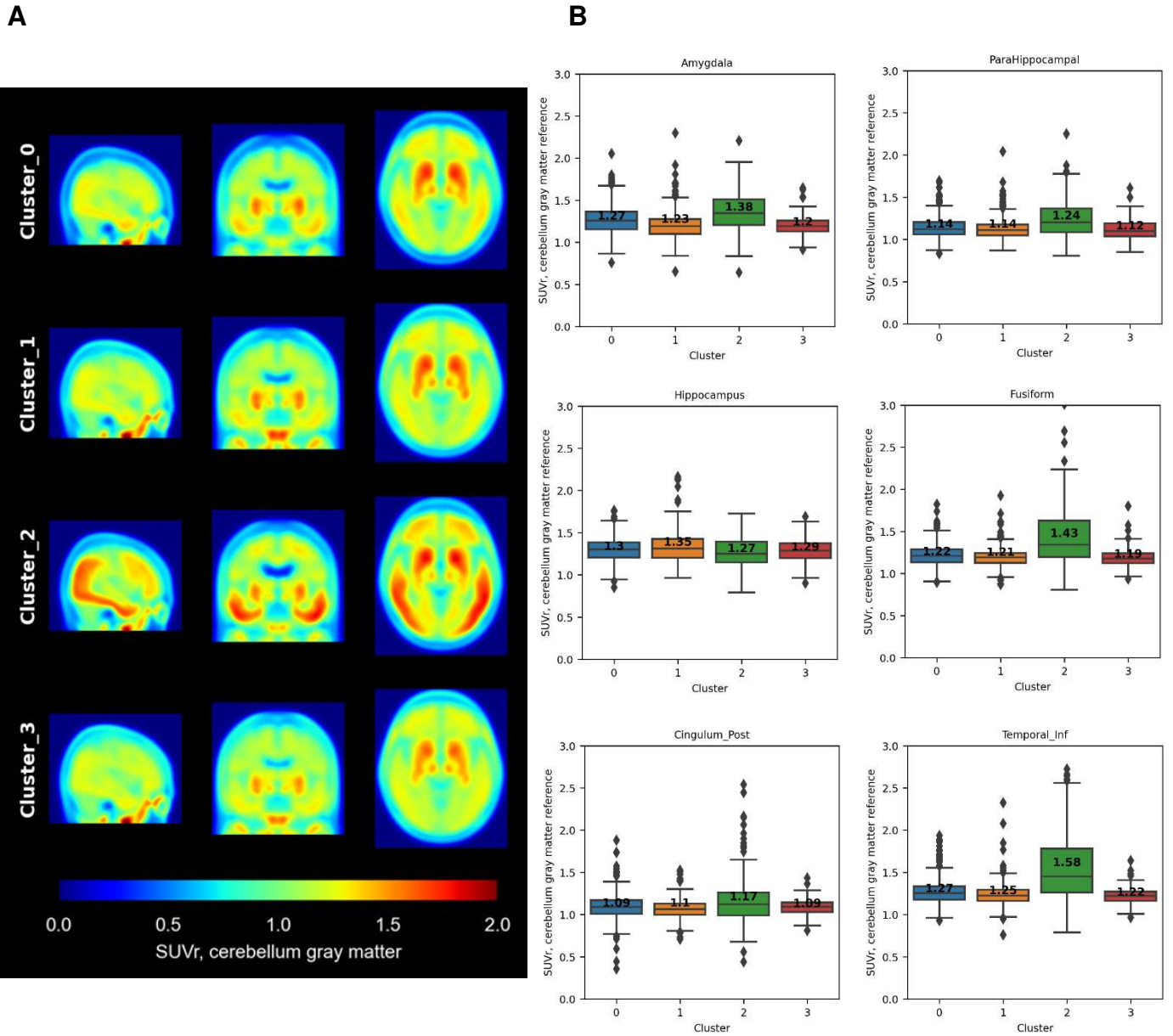


564

Figure 2 Clustering results on t-SNE plot and contingency table. A. t-SNE plot with clustering result. **B.** t-SNE plot with diagnosis. **C.** contingency matrix of cluster result and the diagnosis ratio.

565

566



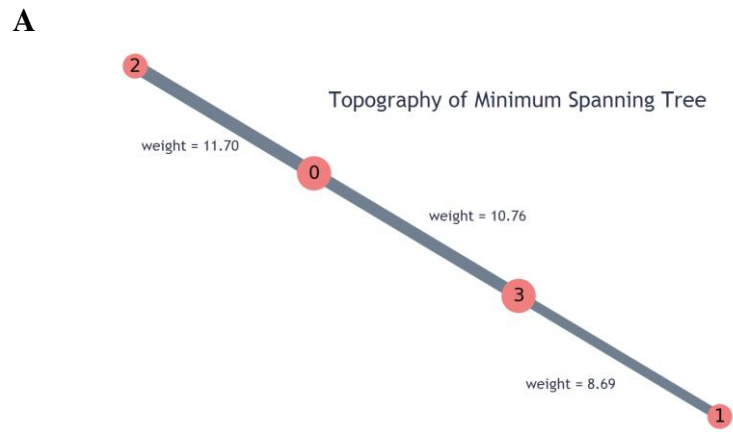
567

568

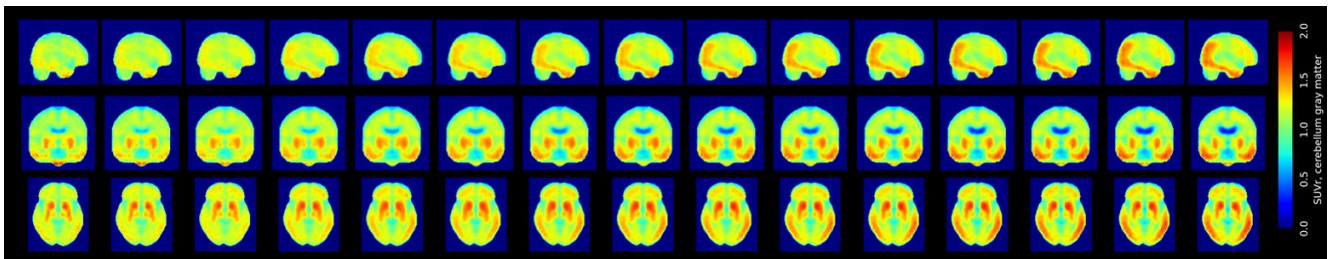
569

Figure 3 Average tau PET image of each cluster. A. The average image of each cluster. Cluster_0 (top), cluster_1, cluster_2, cluster_3 (bottom). **B.** Tau SUVR in temporal and cingulate region. (Amygdala, ParaHippocampal, Hippocampus, Fusiform, Cingulum_post, and Temporal_inf.).

572



B



573

574

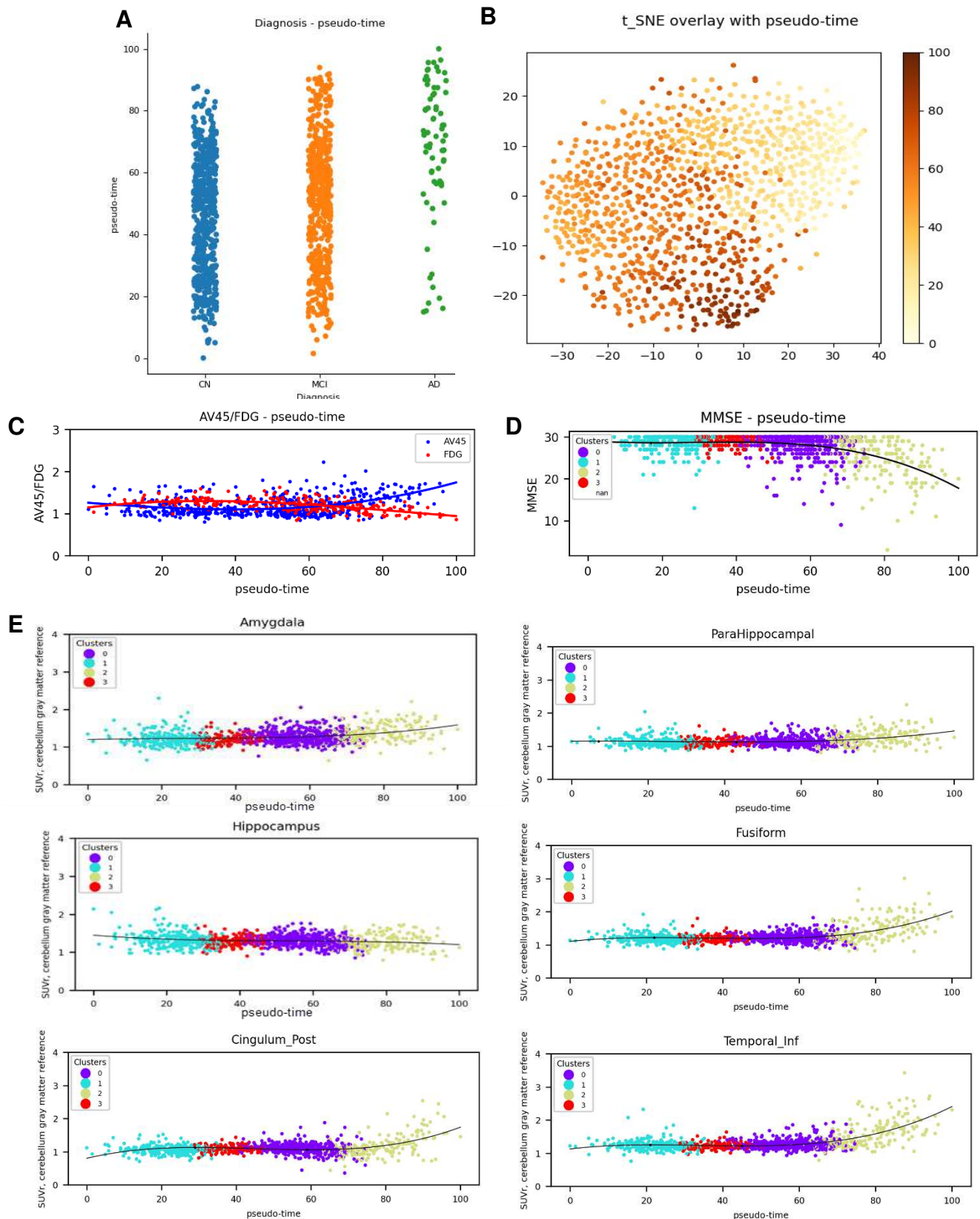
575

576

577

578

Figure 4 Generation of a movie for tau progression pattern using VAE and MST. A. MST graph. The red point depicts the center of cluster. The grey line illustrates the edge with the edge weight. **B.** Tau progression pattern (left to right) generated by the derived MST graph and the trained VAE generator in sagittal (top), coronal, and axial (bottom) view.



579

580

Figure 5 Pseudo-time vs diagnosis/SUVr. A. Pseudo-time vs diagnosis. B. t-SNE plot of pseudo-time. C.

581

Pseudo-time vs [18F]AV45 /FDG. C. Pseudo-time vs MMSE. D. Pseudo-time vs tau SUVr in amygdala,

582

hippocampus, parahippocampal, fusiform, temporal_inf, cingulum_post. Fitted to third degree polynomial

583

illustrated in black curve.

584 **Supplementary Material**

585 **Variational autoencoder (VAE)**

586

587 Given data sample projected in the latent space, z , the probabilistic generator can be
588 expressed as $p_{\theta}(x | z)$. The posterior distribution $p_{\theta}(z | x)$ is obtained by using the prior
589 distribution $p(z)$ and the probabilistic generator $p_{\theta}(x | z)$, such that $p_{\theta}(z | x) \sim p(z)p_{\theta}(x | z)$.

590 The encoder is learns an approximation $q_{\phi}(z | x)$ to the posterior distribution $p_{\theta}(z | x)$, where ϕ
591 denotes the parameters of the encoder, and θ those of the generator. Hence, the VEA loss
592 function used to train the model can be described as,

593
$$L(\phi, \theta) = -E_{z \sim q_{\phi}(z | x)}(\log p_{\theta}(x | z)) + KL(q_{\phi}(z | x) || p_{\theta}(z)).$$

594

595 Note that the first term defines the reconstruction loss, while the second term is acts as
596 a regularization term, in the form of the Kullback-Leibler (KL) divergence between the latent
597 distribution learnt and the prior distribution. In practice, the generator input is resampled by the
598 encoded latent features z ,

599
$$z_{resampled} = z_{encoder} + z_{sd} \times \varepsilon,$$

600

601 where ε represents a random noise sample.

602

603 **Supplementary Table 1** The statistical differences of SUVR in temporal and cingulate ROIs
 604 between each clusters in descending order of F value.

605 *The paired clusters in the square brackets shows significance pair-wise group difference.

606 N.S.: Not significant

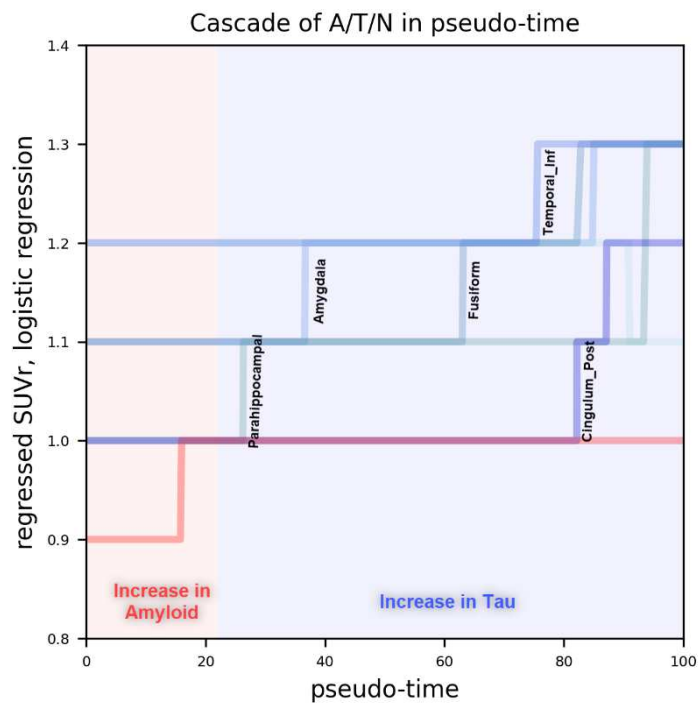
	Cluster 0	Cluster 1	Cluster 2	Cluster 3	F value	p value	*Tukey's test significance
Temporal_Inf	1.27 ±0.14	1.25 ±0.22	1.58 ±0.42	1.22 ±0.1	101.70	< 0.001	[0,2],[1,2],[2,3]
Fusiform	1.22 ±0.13	1.21 ±0.25	1.43 ±0.35	1.19 ±0.11	55.07	< 0.001	[0,2],[1,2],[2,3]
Temporal_Mid	1.17 ±0.13	1.18 ±0.39	1.44 ±0.41	1.17 ±0.09	49.75	< 0.001	[0,2],[1,2],[2,3]
ParaHippocampal	1.14 ±0.13	1.14 ±0.27	1.24 ±0.23	1.12 ±0.11	15.95	< 0.001	[0,2],[1,2],[2,3]
Amygdala	1.27 ±0.17	1.23 ±0.4	1.38 ±0.24	1.2 ±0.13	15.93	< 0.001	[0,2],[0,3],[1,2],[2,3]
Hippocampus	1.3 ±0.14	1.35 ±0.39	1.27 ±0.19	1.29 ±0.14	4.18	< 0.01	[1,2]
Temporal_Sup	1.05 ±0.1	1.09 ±0.66	1.14 ±0.25	1.07 ±0.08	2.69	< 0.1	[0,2]
Heschl	1.04 ±0.1	1.04 ±0.72	1.02 ±0.19	1.02 ±0.08	N.S	N.S	N.S.

607

	Cluster 0	Cluster 1	Cluster 2	Cluster 3	F value	p value	*Tukey's test significance
Cingulum_Mid	1.1 ±0.12	1.09 ±0.38	1.2 ±0.26	1.1 ±0.09	10.19	< 0.001	[0,2],[1,2],[2,3]
Cingulum_Post	1.09 ±0.15	1.1 ±0.51	1.17 ±0.32	1.09 ±0.1	3.51	< 0.03	[0,2],[1,2]
Insula	1.14 ±0.11	1.14 ±0.63	1.17 ±0.23	1.11 ±0.09	N.S	N.S	N.S.
Cingulum_Ant	1.08 ±0.12	1.08 ±0.47	1.07 ±0.22	1.08 ±0.1	N.S	N.S	N.S.

608

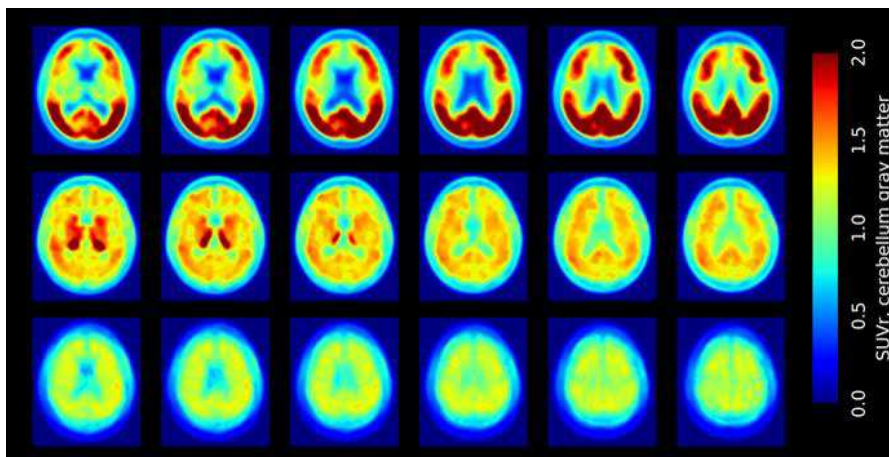
609



610

611 **Supplementary Figure 1** Cascade of amyloid and tau in *pseudo-time*. The rising points of
 612 SUVr of amyloid PET and regional tau PET were estimated by logistic regression.

613



614

615 **Supplementary Figure 2** Examples of outliers which show atypical pattern of tau distribution.
616 Each row is the average image of outliers in cluster 0 (top), cluster 1, and cluster 2 (bottom).

617

Supplementary Files

This is a list of supplementary files associated with this preprint. Click to download.

- [SupFigure1.png](#)
- [SupFigure2.png](#)
- [tautrajectory.mov](#)